DOI: 10.1002/chem.200801215

Interfacial Behavior and Film Patterning of Redox-Active Cationic Copper(II)-Containing Surfactants

Jeffery A. Driscoll,[a] Marco M. Allard,[a] Libo Wu,[b] Mary Jane Heeg,[a] Sandro R. P. da Rocha,*[b] and Cláudio N. Verani*[a]

Dedicated to Professor Ken Karlin for his contribution to copper–pyridine chemistry

Abstract: Herein, we describe the synthesis and characterization of a novel series of single-tail amphiphiles L^{PyC_n} (Py = pyridine, $C_n = C_{18}$, C_{16}, C_{14}, C_{10}) and their copper(II)-containing complexes, which are of relevance for patterned films. The *N*-(pyridine-2-ylmethyl)alkyl-1-amine ligands and their complexes $[Cu^{II}Cl_2(L^{PyC_{18}})]$ (**1**), $[Cu^{II}Cl_2(L^{PyC_{16}})]$ (**2**), $[Cu^{II}Cl_2(L^{PyC_{14}})]$ (**3**), $[Cu^{II}Br_2(L^{PyC_{18}})]$ (**4**), $[Cu^{II}Br_2(L^{PyC_{16}})]$ (**5**), and $[Cu^{II}Br_2(L^{PyC_{10}})]$ (**6**) were synthesized, isolated, and characterized by means of mass spectrometry, IR and NMR spectroscopies, and elemental analysis. Complexes **1**, **2**, **3**, and **6** had their molecular structure solved by X-ray diffraction methods, which showed that the local geometry around the metal center is distorted square planar. With the aim of using these species as precursors for redox-responsive films, an assessment of their electrochemical properties involved cyclic voltammetry in different solvents, with different supporting electrolytes and scan rates. Density functional theory calculations of relevant species in bulk and at interfaces were used to evaluate their electronic structure and dipole moments. The morphology and order of the resulting films at the air/water interface were studied by isothermal compression and Brewster angle microscopy. Biphasic patterned Langmuir films were observed for all complexes except **3** and **6**, and dependence on the chain length and the nature of the halogen coligand determine the characteristics of the isotherms and their intricate topology. Complexes **3** and **6**, which have shorter chain lengths, failed to exhibit organization. These results exemplify the first comprehensive study of the behavior of single-tail metallosurfactants, which are likely to lead to high-end technological applications based on their patterned films.

Keywords: Brewster angle microscopy · copper · Langmuir films · metallosurfactants · redox chemistry

Introduction

Interest in structured and patterned films has increased as a result of their potential for molecular electronics,[1] biosensing,[2] and other high-end technological applications.[3] Similarly, an effort is being made toward understanding the cooperativity between transition-metal ions and amphiphilic organic scaffolds. This interaction leads to redox,[4] optical,[5,6] and magnetic[7] behavior and distinctive order, and has been explored thus far in thixotropic,[8] mesogenic,[9] and micellar[10] design.

Although self-assembly remains the chief approach for film formation,[11–13] isothermal compression[14] allows for greater control over the final morphology.[15,16] This characteristic is fundamental for device nanofabrication, but only in the recent past has the design of amphiphilic precursors departed from lipids to encompass alkylamines,[17] polymers and copolymers,[18] and dendrimers[19] within its subjects. This departure coincides with the availability of surface-dedicated techniques, such as Brewster angle microscopy[20,21] (BAM) and fluorescence microscopy[22] that allow for real-time evaluation of the film compression at the air/water interface.

[a] Dr. J. A. Driscoll, M. M. Allard, Dr. M. J. Heeg, Prof. C. N. Verani
Department of Chemistry
Wayne State University
Detroit Michigan, 48202 (USA)
Fax: (+1) 313-577-8822
E-mail: cnverani@chem.wayne.edu

[b] L. Wu, Prof. S. R. P. da Rocha
Department of Chemical Engineering
Wayne State University
Detroit Michigan, 48201 (USA)
Fax: (+1) 313-577-3810
E-mail: sdr@eng.wayne.edu

Supporting information for this article is available on the WWW under http://dx.doi.org/10.1002/chem.200801215.

The above reasons strongly indicate that understanding how metallosurfactants can drive complex interfacial phenomena, such as morphological changes, domain formation, and collapse mechanisms, with the aim of device development, would constitute a major accomplishment. Nonetheless, with few isolated and characterized precursors,[5,10,23,24] the details of these phenomena are still to be realized.

In recent years, our groups have spearheaded systematic research in this area by focusing on a comprehensive approach that encompasses synthesis,[25] modeling,[26] and surface behavior. We have demonstrated the feasibility of Langmuir–Blodgett (LB) films with magnetic copper(II) clusters,[27] the redox-state control and dependence of a collapse mechanism on cobalt(II) films,[28] and the factor that determines the delicate equilibrium between redox activity and amphiphilicity in copper/phenoxyl species.[29]

Herein, we present an in-depth investigation of the properties of novel single-tail cationic copper(II)-containing surfactants with the ligands $L^{PyC_{18}}$, $L^{PyC_{16}}$, $L^{PyC_{14}}$, and $L^{PyC_{10}}$, in which Py = pyridine and C_n indicates the alkyl chain length.

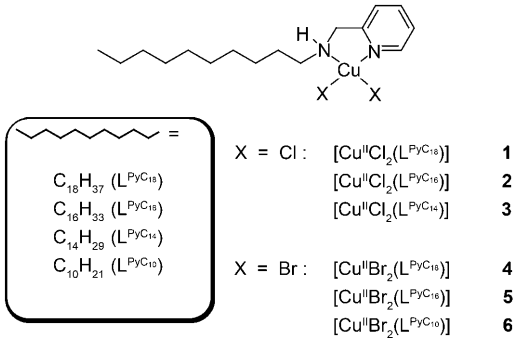

We describe the synthesis and characterization of these new materials along with the molecular structures for **1**, **2**, **3**, and **6**. Examination of their redox properties by using cyclic voltammetry methods relevant for responsive films is presented, along with the behavior at the air/water interface, which was studied by meticulous use of BAM. An assessment of the results supported by density functional theory (DFT) calculations is also included. These findings are expected to have a positive impact on the development of responsive metal-containing LB films in the near future.

Results and Discussion

Synthesis: Treatment of 2-pyridinecarboxyaldehyde with the appropriate alkylamine in methanol gives a Schiff base, which is reduced in the presence of sodium borohydride to give the chelating alkylpyridin-2-ylmethylamine ligands $L^{PyC_{18}}$, $L^{PyC_{16}}$, $L^{PyC_{14}}$, and $L^{PyC_{10}}$ with overall yields of 78–84%. These species were fully characterized by ^{1}H NMR spectroscopy, ESIMS, and IR spectroscopy. The ^{1}H NMR spectroscopic data showed the corresponding protons expected from the combined C–H groups from the pyridine and the alkyl chains, as reported in the Experimental Section. The IR spectroscopic data showed peaks at $\tilde{\nu} = 1484$–$1426\ cm^{-1}$ that were assigned to the stretching vibration of the aromatic C=N$_{Py}$ and C=C bonds, peaks in the $\tilde{\nu} = 2920$–$2850\ cm^{-1}$ range associated with typical alkyl vibrations, and peaks at $\tilde{\nu} = 3306\ cm^{-1}$ that are indicative of the amine nature of the ligand. The ESIMS signals in the positive mode showed peaks with *m*/*z* 361.3, 333.3, 305.3, and 249.3 for $[L^{PyC_n}+H^+]$ for $n = 18$, 16, 14, and 10, respectively. Signal simulation showed excellent agreement with position and isotopic distributions.

Complexes **1**–**6** were all synthesized in a similar manner by treating the appropriate ligand with copper(II) chloride (**1**–**3**) or copper(II) bromide (**4**–**6**), and were isolated as microcrystalline materials and fully characterized. The IR spectra display peaks associated with the ligand, with small shifts indicative of metal coordination. Cu–halogen bonds were not within the detection range.[30] The ESIMS analysis of **1**–**3** in methanol shows peak clusters at *m*/*z* 458.2, 430.2, and 402.2 associated with the $[Cu^{II}Cl(L^{PyC_n})]^+$ fragment, whereas **4**–**6** show equivalent peaks for the $[Cu^{II}Br(L^{PyC_n})]^+$ fragment at *m*/*z* 504.2, 476.2, and 392.3. Each of these cluster peaks display unique profiles related to the presence of isotopic distributions that contain copper (69.2% ^{63}Cu and 30.8% ^{65}Cu), chlorides (75.8% ^{35}Cl and 24.2% ^{37}Cl), and bromides (50.7% ^{79}Br and 40.6% ^{81}Br). Selected examples of such profiles can be seen in Figure 1. All elemental analyses are in excellent agreement with the expected calculated values. Based on the data above, it can be inferred that complexes **1** to **6** are formed by a single ligand coordinated to the copper center and to anionic (Cl^- or Br^-) ligands.

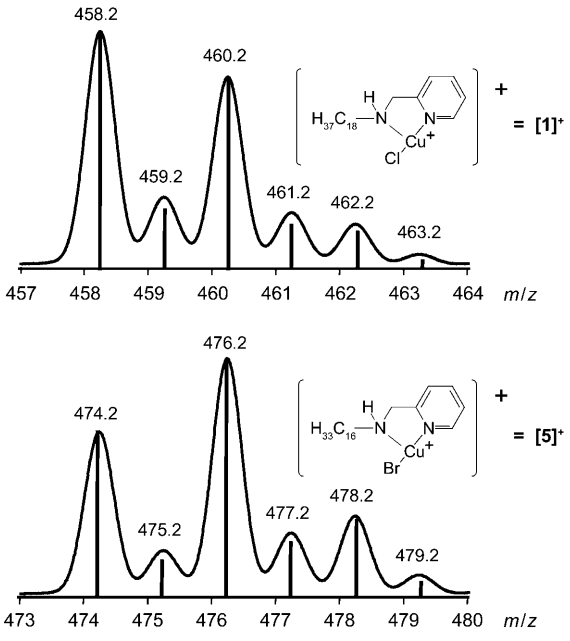

Figure 1. The $[M-X]^+$ ESIMS peak clusters for $\mathbf{1}^+$ (X = Cl^-) and $\mathbf{5}^+$ (X = Br^-). The relative abundance axes are omitted for clarity.

Molecular structures: The molecular structures of **1**, **2**, **3**, and **6** were determined by X-ray crystallography of single crystals obtained from slow evaporation of distinct 1:1 solvent mixtures. Except for the length of the alkyl chain, the chloro-containing complexes **1**, **2**, and **3** display similar general features, including bond lengths and angles. Several attempts to obtain X-ray quality crystals for bromo-containing complexes **4** and **5** failed, but successful molecular structure information was obtained for the analogue complex **6**, which has a $L^{PyC_{10}}$ ligand. Based on complementary techniques, this complex is expected to serve as an accurate model for the geometry adopted by **4** and **5**. The ORTEP diagrams for compounds **1** and **6** are depicted in Figure 2, with selected

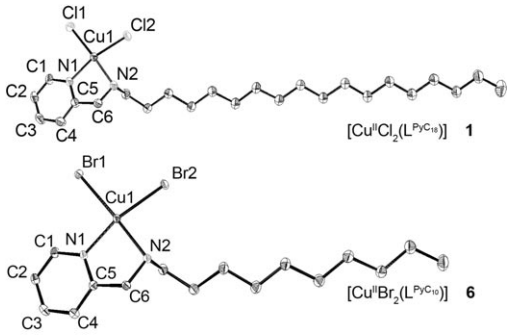

Figure 2. ORTEP diagrams for **1** and **6** with ellipses drawn at the 50% probability level. Selected bond lengths [Å] and angles [°] for **1**: Cu1–N1 = 2.0134(19), Cu1–N2 = 2.028(2), Cu1–Cl1 = 2.2470(6), Cu1–Cl2 = 2.2878(6), C6–N2 = 1.470(3) Å; N1-Cu-N2 = 80.96(8), N1-Cu-Cl1 = 95.69(6), N2-Cu-Cl1 = 176.61(6), N1-Cu-Cl2 = 160.21, N2-Cu-Cl2 = 89.81(6), Cl1-Cu1-Cl2 = 93.54(3)°. Selected bond lengths [Å] and angles [°] for **6**: Cu1–N1 = 2.0142(15), Cu1–N2 = 2.0361(15), Cu1–Br1 = 2.3926(3), Cu1–Br2 = 2.4285(3) Å; N1-Cu-N2 = 81.19(6), N1-Cu-Br1 = 95.89(4), N2-Cu1-Br1 = 176.95(4), N1-Cu1-Br2 = 159.26(5), N2-Cu1-Br2 = 90.05(4), Br1-Cu1-Br2 = 92.996(10)°. See the Supporting Information for details of **2** and **3**.

bond lengths and angles provided. Figures S1 and S2 in the Supporting Information present data for **3** and **4**. Species **1**, **2**, and **3** crystallize in the triclinic space group $P\bar{1}$ and consist of discrete and neutral molecules with a CuN_2Cl_2 coordination sphere. The Cu–N_{Py} bond lengths for these species vary between 2.007 and 2.013 Å, whereas the Cu–N_{amine} bond lengths are 2.028 to 2.032 Å. Two *cis*-oriented chloro ligands complete the coordination sphere around the metal ion. The bond length of one of the chloro ligands is slightly shorter at about 2.25 Å, whereas the other Cu–Cl length is about 2.29 Å. The bite angles of the amine and pyridine nitrogen atoms from the L^{PyC_n} ligand coordinated to copper are about 81° and the Cl-Cu-Cl angles exceed 90°, whereas the N-Cu-Cl angles exceed 160°. This reinforces the notion of a distorted square planar environment that is favored for bivalent copper ions because considerable deviation occurs from the 90° expected in a perfect square planar geometry.[31,32]

Complex **6** also presents a triclinic $P\bar{1}$ space group and has a local CuN_2Br_2 coordination sphere with slightly longer Cu–N bonds due to the presence of bulkier bromo ligands. One of the Cu–Br bonds is comparable to the Cu–Cl bonds described above, whereas the other one is longer with a length of 2.43 Å. These bond lengths are in good agreement with reported values.[33,34]

All of the above species are loosely associated in the solid state as $[Cu^{II}(L^{PyC_n})X_2]_2$ ($X = Cl^-$, Br^-) dimers through long Cu···X′ bonds (2.75 and 2.93 Å for Cl′ and Br′, respectively; see Figure S1 in the Supporting Information). This weakly bound dimer readily dissociates in solution, as evidenced by EPR spectroscopy and ESIMS measurements at low cone voltage. The hydrocarbon chains in all of the above species present an average C–C bond length of 1.52 Å, whereas the average C–C ring bond length is 1.48 Å.

Redox properties of the precursors: To develop responsive films, a thorough understanding of the redox properties of the precursors is needed. Several compounds were scanned in acetonitrile to assess the redox potentials of the copper ion. It was observed that the length of the alkyl chains has a negligible effect on the potentials, thus suggesting an absence of ligand-inductive effects or decreasing rates of interfacial electron transfer.[35] Compounds **1** and **5** were selected and studied in a range of solvents with distinct polarities and with different supporting electrolytes. The results allow us to present an accurate picture regarding their redox potentials, reversibility, and cyclability. The two supporting electrolytes used were tetrabutylamonium hexafluorophosphate ($TBAPF_6$) and perchlorate ($TBAClO_4$), which were chosen with the aim of observing how they favor electrochemical reversibility.[36] The solvents were dichloromethane, acetonitrile, and dimethylformamide. Several scan rates were probed and the best reversibility was attained at 150 $mV\,s^{-1}$. Table 1 summarizes the results, with all potentials reported versus the Fc^+/Fc couple. No formation of metallic copper was observed.

The $3d^9$ copper(II) ion has a flexible coordination sphere that favors square planar, square pyramidal, or trigonal bipyramidal geometries, whereas the reduced copper(I) counterpart, which has a $3d^{10}$ configuration, prefers a tetrahedral geometry.[37] Because of this geometrical reorganization during the redox process, an irreversible behavior is expect-

Table 1. Cyclic voltammetry data for **1** and **5**.[a]

Compound	Solvent	Electrolyte	$E_{1/2}$ (ΔE_p) [V]	$\lvert I_{pc}/I_{pa}\rvert$
$[Cu^{II}Cl_2(L^{PyC_{18}})]$ (**1**)	DCM	$TBAPF_6$	−0.70 (0.24)	1.2
	DCM	$TBAClO_4$	−0.74 (0.23)	1.9
	ACN	$TBAPF_6$	−0.48 (0.16)	1.3
	ACN	$TBAClO_4$	−0.54 (0.29)	2.5
$[Cu^{II}Br_2(L^{PyC_{16}})]$ (**5**)	DCM	$TBAPF_6$	−0.73 (0.17)	1.6
	DCM	$TBAClO_4$	−0.75 (0.20)	1.2
	ACN	$TBAPF_6$	−0.51 (0.13)	1.5
	ACN	$TBAClO_4$	−0.52 (0.15)	1.4
	DMF	$TBAPF_6$	−0.55 (0.20)	2.4
	DMF	$TBAClO_4$	−0.55 (0.24)	2.1

[a] Room temperature measurements. Potentials are referenced versus the Fc^+/Fc couple (Fc = ferrocene). Individual $\Delta E_{Fc^+/Fc}$ values range from 0.09 to 0.11 V.

ed. Therefore, it is somewhat surprising that both **1** and **5** display quasi-reversible behavior at low potentials.

As can be seen in Figure 3, compound **1** shows limited reversibility. In dichloromethane (data not shown), peak separations (ΔE_p) greater than 0.20 V suggest near irreversible

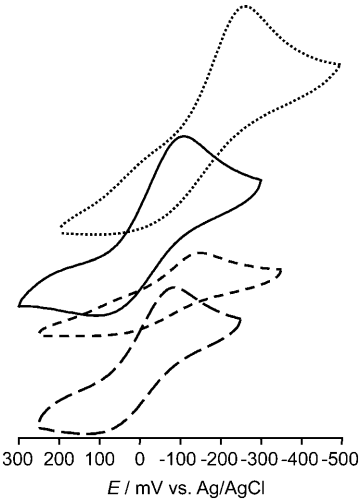

Figure 3. Selected cyclic voltammograms for 1.0×10^{-3} M solutions of **1** and **5** in acetonitrile with different supporting electrolytes. •••••: **1** with $TBAClO_4$, ——: **5** with $TBAClO_4$, -----: **1** with $TBAPF_6$, – – –: **5** with $TBAPF_6$.

behavior. In acetonitrile, when $TBAClO_4$ is present the value of ΔE_p is about 0.30 V and $|I_{pc}/I_{pa}|>2.0$, which indicates an irreversible process. Changing the supporting electrolyte to $TBAPF_6$ decreases ΔE_p to half the previous value, which suggests quasi-reversible behavior that is also supported by an $|I_{pc}/I_{pa}|$ value that approaches unity. The coordinating nature of dimethylformamide was thought to help stabilize the redox processes observed for **5**. However, an irreversible behavior was observed with values of $\Delta E_p \approx 0.20$ V and $|I_{pc}/I_{pa}|$ values greater than 2.0.

Acetonitrile seems to foster similar $E_{1/2}$ values independent of the supporting electrolyte, and ΔE_p values of ≈ 0.20 V and $|I_{pc}/I_{pa}| \approx 1.5$ also attest for the quasi-reversible nature of the Cu^{II}/Cu^{I} couple. The opposite was observed when noncoordinating dichloromethane was used. The nature of the electrolyte leads to smaller peak separations associated with larger $|I_{pc}/I_{pa}|$ values.

In an attempt to generalize these observations, the following conclusions can be drawn: 1) The presence of halides leads to quasi-reversible redox processes, 2) the redox processes of chloro-containing **1** are less reversible than bromo-containing **5**, 3) the use of $TBAPF_6$ as the electrolyte favors smaller ΔE values within quasi-reversible ranges, and 4) acetonitrile supports better reversibility, followed by dichloromethane and then dimethylformamide.

It is suggested that this observed quasi-reversibility is related to the unique coordination spheres of **1** and **5**, which have both halogen and pyridine donors. Chlorocopper(II) systems $[Cu^{II}Cl_4]^{-2}$, $[Cu^{II}Cl_3(S)]^{-}$, and $[Cu^{II}Cl_2(S)_2]^{0}$ (S = solvent) are expected to be square planar, but tend to be tetrahedral in solvents with high dielectric constants and high donor number, such as acetonitrile.[37,38] Similarly, the presence of PF_6^- counterions leads to distorted planar geometry in environments with similar denticity and structure as those of $L^{PyC_{16}}$ and $L^{PyC_{18}}$.[39] Therefore, **1** and **5** deviate considerably from the expected square planar geometry, both as solids (see the structural data) and in solution. Consequently, the $3d^9 \rightleftarrows 3d^{10}$ reorganization becomes energetically affordable and gives the observed quasi-reversible processes.

Amphiphilic properties and film patterning: To evaluate the amphiphilic behavior of **1**–**6**, the resulting Langmuir monolayers were studied by surface pressure versus area (Π vs. A) isotherms and BAM. Compression isotherms give information about the 2D behavior of the resulting Langmuir film at the air/water interface, the presence of mesophasic changes, the collapse pressure (π_c), and the average area per molecule at the collapse of the monolayer at collapse (A_c). The surfactant is initially dissolved in an immiscible organic solvent, such as chloroform, and subsequently spread on the water surface. As the barriers of the trough are compressed, the tension (γ) of the air/water interface in the presence of the amphiphilic species decreases as compared with that of the bare air/water interface ($\gamma_0 = 72$ mN m^{-1} at 23 °C), resulting in an increase in Π ($=\gamma_0-\gamma$). Figure 4 shows the results for ligand $L^{PyC_{18}}$ and its chloro (**1**) and bromo (**4**) copper-containing analogues (top), and $L^{PyC_{16}}$ and its derivatives **2** and **5** (Figure 4, bottom). It is worth noting that $L^{PyC_{14}}$, $L^{PyC_{10}}$, **3**, and **6** were unable to form organized films at the air/water interface. Based on their erratic behavior under compression, it can be concluded that these species dissolve in the subphase. Further studies involving light scattering are

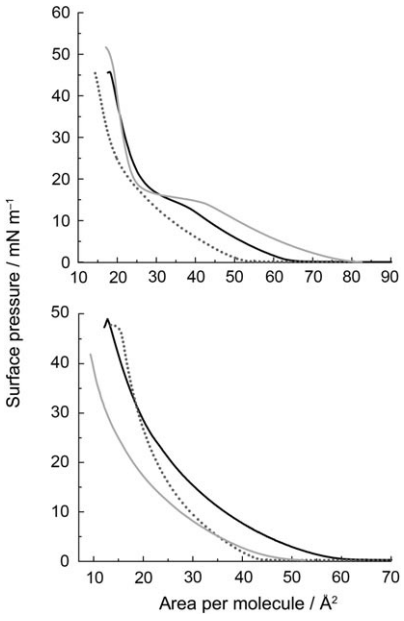

Figure 4. Pressure versus area isotherms of a) ligand $L^{PyC_{18}}$ (——) and its copper complexes **1** (——) and **4** (•••••), and b) ligand $L^{PyC_{16}}$ (——) and its copper complexes **2** (——) and **5** (•••••).

currently under development to determine the appropriate mechanisms. The compression isotherms of ligands $L^{PyC_{18}}$ and $L^{PyC_{16}}$ are discussed below and reveal intrinsic differences. Ligand $L^{PyC_{18}}$ exhibited a typical uneventful compression at low pressures with average areas per molecule reaching 70–80 Å^2, which reflects a lack of organization. As the pressure increased, the ligand underwent a phase transition at 13–17 mN m^{-1} analogously described as a gas-to-liquid transformation. This can be attributed to an increased repulsion between the individual molecules on the surface. A steeper slope was observed after this transition. The average area per molecule at collapse (A_c) was obtained by extrapolating the steepest part of the curve down to zero pressure.[3,14] The pyridine head-group of the ligand seems to have interfered little with the packing of the monolayer, and the observed area of 23–25 Å^2 molecule^{-1} is comparable to the packing reported for a carboxylic acid with an equivalent number of carbon atoms.[40] The formal film collapse happened at 45–50 mN m^{-1}. Unlike $L^{PyC_{18}}$, ligand $L^{PyC_{16}}$ does not display any phase transitions and collapses at around 40 mN m^{-1} with similar average areas per molecule. It is clear that the average areas at collapse should be similar, and that the plateaulike phase transition for the former ligand must be related to the presence of longer alkyl chains and their organization on the surface. Events related to this behavior might be associated with the configuration and the presence of different degrees of defects in the chains. Complex **1** reinforces this notion by displaying a similar overall behavior with a comparable plateau from 12–18 mN m^{-1} and an average area of 30–31 Å^2. A more expanded isotherm is expected after the addition of a bulky and charged copper cation. Interestingly, if the chloro ligands in **1** are replaced by bromo ligands in **4**, this phase transition disappears almost completely and smaller average areas of 25–27 Å^2 are observed. Intuitively, it would seem that bromo-substituted **4** should have a greater area per molecule than its chloro-substituted counterpart **1**. However, the polarizability of the bromides might allow for improved solubility into the subphase, which would lead to higher organization of the aliphatic chains. In spite of the expected dynamic equilibrium at the interface, the relative geometry of the polar metal-containing head group should also be considered; assuming the higher mass and polarizability of the bromo ligands, a more pronounced tetrahedral character could be favored in solution, whereas the chloro-containing **1** would be less distorted. The inclusion of metals to $L^{PyC_{16}}$ gives **2** and **5**, but similarly to the ligand, neither species exhibits obvious phase transitions in their isotherms. Overall, the C_{16} species start organizing at lower area per molecule values and collapse at slightly lower pressures than their C_{18} counterparts, which thus reflects the influence of the chain length. In contrast to **1** and **4**, species **2** and **5** display similar A_c values of 26–28 Å^2 at collapse, with **5** showing a steeper slope. The reported collapse pressures for **1**, **2**, **4**, and **5** are significantly greater than those observed for other metal–surfactant complexes. However, the A_c increase is less noticeable than that of a phenanthroline-based surfactant upon copper insertion,[41] but is significantly smaller than that of a bipyridylrhenium(I) surfactant[5b] with the same hydrocarbon chain length. Comparison with another recently published cuproamphiphile,[29] in which the surfactant head group is a *tert*-butyl-substituted phenolate, also suggests that the pyridine-based systems give higher collapse values and more organized films. Differences in the ligand head groups, the oxidation states of the ions, and their electronic structures explain the significant variation in A_c between the 3d copper(II) and the 5d rhenium(I) surfactants.

BAM studies: BAM uses polarized light passing through media with dissimilar refractive indexes and is the most powerful method available to identify structures such as agglomerates and domains in films at the air/water interface.[42] The compression of films has been investigated for $L^{PyC_{18}}$, **1**, and **2**, and also $L^{PyC_{16}}$, **4**, and **5** to assess the dynamics of phase change and domain formation and to gain insight in the behavior observed during the isothermal compression experiments discussed above. Selected images for $L^{PyC_{18}}$, **1**, and **2** are shown in Figure 5. Beginning with ligand $L^{PyC_{18}}$

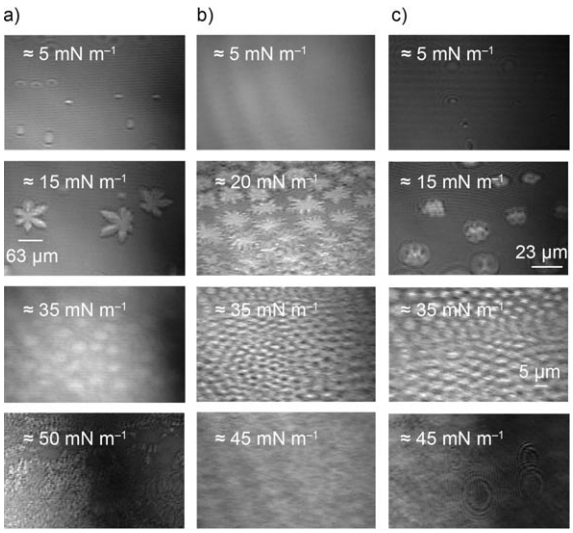

Figure 5. Selected BAM micrographs of a) ligand $L^{PyC_{18}}$, b) **1**, and c) **4**.

(Figure 5a), compression at 5 mN m^{-1} showed a homogeneous surface with sporadic Newton circles,[43] which were attributed to multilayer granule formation from ejection of matter due to localized oscillations. As the lateral compression continued, the pressure increases prompted the ligand to undergo a 2D liquid–gas phase transition (13–15 mN m^{-1}). At this point, nucleation led to a condensed leaflike domain formation. These domains resemble side-branching morphologies that have been observed for other secondary amines, such as dioctadecylamine.[44] As compression was continued beyond the plateau, the number of domains quickly increased, whereas an overall decrease in size from ≈63 to 25 µm was observed. Around 35–40 mN m^{-1}, the interspatial distance decreased to the point that a homo-

geneous film was formed and continued through collapse at 50 mN m^{-1}. The BAM micrographs for chloro-containing **1** are shown in Figure 5b and start with a homogeneous monolayer that subexists up to 8–9 mN m^{-1}, at which point domain formation begins and coincides with the region that precedes the plateau observed in the isotherm of the compound. From this plateau onward, the emerging domains adopt five- to seven-fold branched star-shaped morphology and continue to develop throughout compression. The domains decrease in size at higher surface pressures, and display more ordered spherical morphologies until the surface reaches relative homogeneity prior to collapse at 45 mN m^{-1}. Interestingly, the film of bromo-containing **4** (Figure 5c) shows the formation of a homogeneous film up to 9–12 mN m^{-1} with sporadic Newton rings. In good agreement with the lack of a plateau in its isotherm, no formation of branched star-shaped domains was observed. Only small and sparse spherical domains were observed at 15–20 mN m^{-1}, and at higher surface pressures (35 mN m^{-1} and upwards) these domains decreased in size and led to homogeneity. At higher surface pressures, similar film topologies were observed for **4** and **1**. The higher the compression becomes, the smaller the interspatial distance between the resulting domains, which leads to comparable collapse pressures and morphologies. It has been suggested by Vollhardt and Wiedemann[45] that the growth of these structures is due to domain crowding from supersaturation on the surface of the surrounding phase. Additionally, we hypothesize that a dynamic equilibrium exists between the dihalogenated species $[Cu^{II}(L^{PyC_n})X_2]$ and their monohalogenated and solvated analogues $[Cu^{II}X(H_2O)(L^{PyC_n})]^+$ and $[Cu^{II}(H_2O)_2(L^{PyC_n})]^{2+}$ at the air/water interface. Each of these species should display distinct dipole moments that increase molecular motion. Formation of domains would, therefore, be a mechanism to stabilize the film by decreasing mobility.

During lateral compression of the ligand $L^{PyC_{16}}$, no clear plateau comparable to that of $L^{PyC_{18}}$ was observed. A well-organized monolayer was detected up to 8 mN m^{-1}, with few Newton circles appearing slightly above 9 mN m^{-1}. Nucleation and domain formation started to appear at 16 mN m^{-1}. At 21 mN m^{-1}, round flowerlike domains (see Figure S3 in the Supporting Information) were formed and combined without reverting back to the initial homogeneous film exhibited early in the experiments. These domains do not resemble the side-branched leaflike domains observed for $L^{PyC_{18}}$, and seem to have a tip-splitting morphology.[44] This suggests that the shorter alkyl chain length of the ligand dictates the resulting pattern of the condensed phase. It would be interesting to compare different lengths of alkyl chains, but it has been observed that chains shorter than hexadecane (C_{16}) are dissolved in the subphase under the current experimental conditions. Similarly to $L^{PyC_{16}}$, the isotherm of **2** does not display an apparent plateau, and a homogeneous film without domain formation was observed up to 24 mN m^{-1}. The addition of a metal to the ligand and the presence of halogeno coligands permitted the monolayer to withstand nearly three times the surface pressure of the non-metalated species. At 25 mN m^{-1}, oscillations associated with possible film buckling appeared. Nonhomogeneous spherical domains began to form and continued through collapse at around 50 mN m^{-1}. Compound **5** showed similar isotherms as the ligand and chlorinated species. Nonetheless, a homogeneous film was observed and domains were not detected throughout the lateral compression stage up to the collapse point. As previously suggested, the aliphatic chains must exhibit high interaction energies to provide ordered liquid-condensed-phase monolayers.[46] Furthermore, a delicate balance between the selection of the coligands and the length of the alkyl chains seems to exist, and appears pivotal to the control of domain formation in Langmuir films of these metallosurfactants. In these experiments, surface pressure was the only variable. Domain morphology can also be influenced by factors such as distinct compression rates, time and temperature changes, and subphase modification.[17,44,47,48] Ongoing work in our labs focuses on these factors. Similarly, to assess the relationship between domain formation and degree of disorder, a detailed study based on atomic-force microscopy and sum frequency generation vibrational spectroscopy is currently underway.

Electronic structure calculations: A series of electronic structure calculations were carried out on simplified models to evaluate our explanations about the electrochemical and amphiphilic behavior of the copper precursors **1**–**6**. Figure 6a shows the models we used, which consist of aminomethylpyridine head groups with shorter ethyl chains. These simplified ligands are coordinated to copper and chloro groups as in $[Cu^{II}Cl_2(L^{PyC_n})]$ to mimic compounds **1**–**3**, and bromo groups as in $[Cu^{II}Br_2(L^{PyC_n})]$ to mimic **4**–**6**. A model in which one chloro group is replaced by water, described as $[Cu^{II}Cl(H_2O)L]^+$, was considered; this is the most likely species to be in equilibrium with $[Cu^{II}Cl_2L]$ at the air/water interface. Another model, $[Cu^{II}(H_2O)_2L]^{2+}$, was included for comparison purposes, in spite of the fact that its concentration is not expected to be significant because the stabilization of the 2+ charge would be energetically demanding when chloride ions are present. In general terms, it can be seen that all species exhibit a SOMO with distinctive metal character. This orbital is best described as the $d_{x_2-y_2}$ orbital, which interacts in a σ fashion with the p-type orbitals of the halogen and nitrogen donors, as shown in Figure 6b. In idealized N_4 square planar environments, this would correspond to the antibonding b_{1g} molecular orbital.[49] However, compounds **1**–**6** have $NN'Cl_2$ and $NN'Br_2$ coordination environments, and therefore, much lower symmetry. Considering equivalency between the amine and pyridine nitrogen atoms would lead to N_2Cl_2 and N_2Br_2 environments of approximate C_2 symmetry. In that case, the SOMOs should be labeled as *a*. Because more elaborate calculations would be required to ascertain the answer to this question, the discussion will be restricted to the relative energies of the highest occupied molecular orbital (HOMO, which herein coincides with the SOMO) and the lowest unoccupied molecular orbital (LUMO). The influence of the different monodentate li-

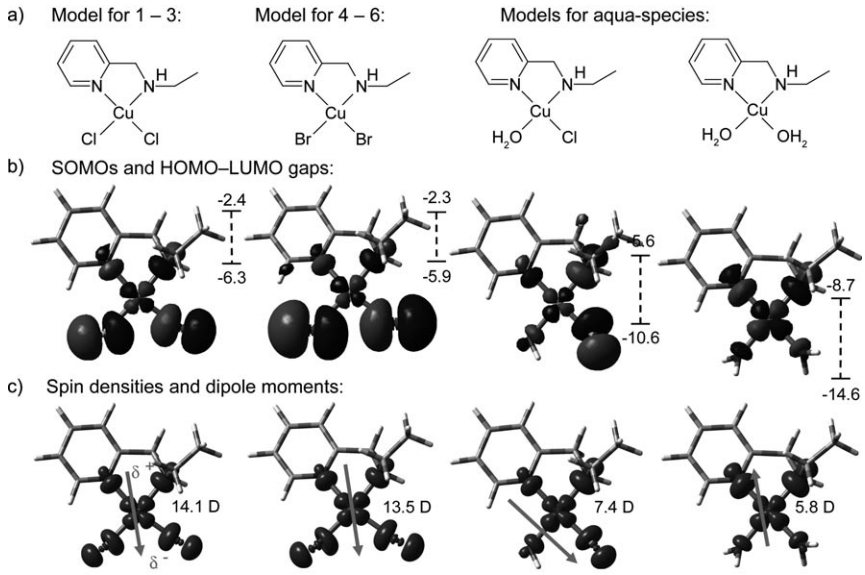

Figure 6. a) Simplified models of the surfactants, b) Singly occupied molecular orbitals (SOMOs) for these models, and c) spin-density plots.

gands (Cl^-, Br^-, and H_2O) on the energy of the HOMO and the HOMO–LUMO gap is dramatic. Following an arbitrary scale, as shown in Table 2, the $[Cu^{II}Cl_2L]$ and $[Cu^{II}Br_2L]$ species display comparable gaps of 3.6 to 3.9 eV, whereas $[Cu^{II}Cl(H_2O)L]^+$ and $[Cu^{II}(H_2O)_2]^{2+}$ show more pronounced values of 5.0 to 5.9 eV due to the presence of positive charges.

Table 2. Electronic structure parameters.

Compound	HOMO [eV]	LUMO [eV]	Electron affinity [eV]	Dipole moment [D]
$[Cu^{II}Cl_2L]$	−6.3	−2.4	1.2	14.1
$[Cu^{II}Br_2L]$	−5.9	−2.3	1.3	13.5
$[Cu^{II}Cl(H_2O)L]^+$	−10.6	−5.6	5.0	7.4
$[Cu^{II}(H_2O)_2L]^{+2}$	−14.6	−8.7	9.1	5.8

It is assumed that the $Cu^{II} \rightarrow Cu^{I}$ reduction processes will depend mainly upon the relative energies of the SOMO orbitals of the bivalent $3d^9$ metal complex. Therefore, for the formation of a $3d^{10}$ Cu^I species by the addition of one electron, the vertical electron affinity is the best parameter for comparison. The affinity for $[Cu^{II}Cl_2L]$ and $[Cu^{II}Br_2L]$ was calculated and found to be 1.2 and 1.3 eV, respectively, which leads to the conclusion that $[Cu^{II}Br_2L]$ should have a more energetically favorable reduction. As such, this is in excellent agreement with the observed electrochemical data, in which compound **5** displays slightly more affordable reductions than **1**. Therefore, it is expected that $[Cu^{II}Cl(H_2O)L]^+$ would display more positive potentials. As can be observed in Figure 6c the spin-density plots and the orientation of the dipole moments are provided. The spin density reinforces the notion that the unpaired electron of each model does correlate to the SOMO, and that this shows a $d_{x_2-y_2}$ character, as proposed previously. Equally interestingly, the analysis of the dipole moments may allow for the discussion of the observed behavior in Langmuir films. Models for the nonmetalated ligand show a dipole moment of 2.09 D, whereas $[Cu^{II}Cl_2L]$ and $[Cu^{II}Br_2L]$ show higher but similar dipole moments of 13–14 D. The value observed for the ligand is comparable to that of pyridine alone (2.30 D),[50] and upon metalation the chloro species displays a slightly higher value than the bromo species. This is consistent with the electronegativity trend for the halogen atoms. A considerable difference is seen when $[Cu^{II}Cl_2L]$ is compared to $[Cu^{II}Cl(H_2O)L]^+$, in which the replacement of a chloro group results in a dramatic decrease in the original dipole moment value to about half. This decrease is also followed by a change in the direction of the vector. In the event that $[Cu^{II}(H_2O)_2L]^{2+}$ would form in appreciable concentrations, an inversion of the dipole takes place. A picture of the dynamic character of the films can be drawn, when considering these species, and the equivalent bromo-substituted ones, at the air/water interface. Because the $[Cu^{II}Cl_2L] \rightleftarrows [Cu^{II}Cl(H_2O)L]^+$ and, to a lesser extent, the $[Cu^{II}Cl(H_2O)L]^+ \rightleftarrows [Cu^{II}(H_2O)_2L]^{2+}$ equilibria are supposed to occur quickly, the dipole moment of these species will be changing constantly. The change is followed by molecular rearrangements at the air/water interface, which can trigger aggregation and domain formation as the surface pressure changes.

Conclusion

Herein we have synthesized and characterized a series of novel surfactants and metallosurfactants. New pyridine-based ligands L^{PyC_n} ($C_n = C_{18}$, C_{16}, C_{14}, C_{10}) were treated with halogeno-copper(II) salts to give compounds **1**–**6**, described as $[Cu^{II}(L^{PyC_n})X_2]$. Compounds **1**, **2**, **3**, and **6** had their molecular structure solved by X-ray diffraction methods, which showed that the local geometry around the metal center is distorted square planar. The electrochemical behavior of these species revealed that the unique coordination sphere, which contains halogen atoms and pyridines, leads to quasi-reversible—rather than the expected irreversible—redox processes. This property is enhanced in bromo-substituted species in acetonitrile if $TBAPF_6$ is used as the supporting electrolyte. These results were partially supported by DFT-based vertical electron affinity calculations that suggest a more energetically favorable reduction for bromo-substitut-

ed models. Isothermal compression revealed that longer chain lengths, such as -$C_{18}H_{37}$ in $L^{PyC_{18}}$ and **1**, lead to the formation of a plateau that corresponds to a biphasic film. On the other hand, chain lengths like -$C_{16}H_{33}$ in $L^{PyC_{16}}$, **2**, and **5** do not display such obvious mesophasic change. The effect of the chain length seems to be overcome by the nature of the anionic coligand because the larger bromo complex in **4** lacked the expected plateau. This was attributed to a higher subphase solubility compared to that of the chlorinated complexes. Furthermore, variation of the chain length in absence of the metal ion dictates the morphological characteristics on the condensed domains. The metalated complexes provide more homogeneous monolayer formation at significantly higher pressures compared with the ligands alone. Finally, chain lengths shorter than $C_{16}H_{33}$ (as seen in **3** and **6**) typically failed to exhibit any organization at the air/water interface under the current experimental settings. Although the lack of a larger body of work prevents us from attempting generalizations for metallosurfactants in general, these results exemplify the first detailed study on the behavior of single-tail copper surfactants at the air/water interface and as solid films. The analysis of calculated dipole moments was used to rationalize the behavior observed in Langmuir films, in which models of the ligands showed dipole moments comparable to that of pyridine. The metal-containing complexes displayed considerably higher dipole moments that indicated the efficacy of metalation as a tool for surfactant design. The equilibrium between dihalogenated complexes and monohalogenated/solvated complexes results in dynamic changes in the dipole moment, which leads to the biphasic topologies observed experimentally. On the basis of these observations, we can conclude that the behavior of metallosurfactants is unique and can be modulated further, thereby leading to a general strategy for morphological control. Thus, it can be envisioned that customized film patterning can and will be useful for the design of LB-based devices that take advantage of the intrinsic properties of metal centers. Ongoing research in our labs is focused on the development of a broader selection of metallosurfactants, such as iron and cobalt analogues, and on the alteration of deposition conditions, such as temperature and compression rate. The inclusion of different ions is aimed at redox reversibility and spin-crossover properties, whereas the changing deposition methods focus on the control of the patterning phenomenon.

Experimental Section

Materials and methods: All the reagents were obtained from commercial sources and were used without further purification. Dichloromethane was purified by using an I.T. solvent purification system. ^{1}H NMR spectra were recorded by using a Varian 400 MHz instrument. IR spectra were measured from $\tilde{\nu}=4000$ to 400 cm^{-1} by using KBr pellets on a Tensor 27 FTIR-spectrophotometer. ESIMS were measured on a Micromass QuattroLC triple quadrupole mass spectrometer equipped with an electrospray/APCI source, Waters Alliance 2695 LC autosampler, and photodiode array UV detector. Experimental assignments were simulated based on signal position and isotopic distributions. Elemental analyses were performed by Midwest Microlab, Indianapolis, Indiana. Cyclic voltammetry experiments were performed by using a BAS 50W voltammetric analyzer. A standard three-electrode cell was employed with a glassy carbon working electrode, a Pt wire auxiliary electrode, and an Ag/AgCl reference electrode under an inert atmosphere at RT. Potentials are presented versus Fc^+/Fc[51] as the internal standard. Dry dichloromethane, acetonitrile, and dimethylformamide were used as the solvents. The concentration of the analytes was 1.0×10^{-3} M and the concentration of the supporting electrolytes $TBAPF_6$ and $TBAClO_4$ was 0.1 M. Experiments were run at scan rates of 50, 100, 150, 200, and 300 mV s^{-1}.

X-ray structural determination for 1, 2, 3, and 6: Diffraction data for complex **1** were collected on a Bruker P4/CCD diffractometer equipped with $Mo_{K\alpha}$ radiation and a graphite monochromator at 213 K. Data were measured at 10 s $frame^{-1}$ with 0.3° between frames. Diffraction data for the remaining three structures (**2**, **3**, and **6**) were measured on a Bruker APEX-II kappa geometry diffractometer with $Mo_{K\alpha}$ radiation and a graphite monochromator at 100 K. Frames were collected with the detector at 40 mm, 0.3° between each frame, and 5–10 s $frame^{-1}$. All frame data were indexed and integrated by using the manufacturer's SMART, SAINT, and SADABS software.[52] The models were refined by using Sheldrick's SHELX-97 software.[53] A summary of the crystal structure parameters is shown below. These four complexes crystallize as dimers through an inversion center, with long axial Cu···X interactions and N−H···X hydrogen bonds.

Complex ***1***: Formula = $C_{48}H_{88}N_4Cl_4Cu_2$; $M_r=990.10$; space group = $P\bar{1}$; $a=7.5068(8)$, $b=9.7426(12)$, $c=19.250(2)$ Å; $\alpha=90.194(2)$, $\beta=98.838(2)$, $\lambda=109.470(2)°$; $V=1309.4(3)$ Å^3; $Z=1$; $T=213(2)$ K; $\lambda=0.71073$ Å; $\rho_{calcd}=1.256$ g cm^{-3}; $\mu=1.051$ mm^{-1}; $R(F)=3.64\%$; $wR(F)=8.63\%$.

Complex ***2***: Formula = $C_{44}H_{80}N_4Cl_4Cu_2$; $M_r=934.00$; space group = $P\bar{1}$; $a=7.4943(10)$, $b=9.7419(12)$, $c=17.533(2)$ Å; $\alpha=98.810(6)$, $\beta=94.108(7)$, $\lambda=108.915(6)°$; $V=1186.5(3)$ Å^3; $Z=1$; $T=100(2)$ K; $\lambda=0.71073$ Å; $\rho_{calcd}=1.307$ g cm^{-3}; $\mu=1.155$ mm^{-1}; $R(F)=2.91\%$; $wR(F)=7.22\%$.

Complex ***3***: Formula = $C_{40}H_{72}N_4Cl_4Cu_2$; $M_r=877.90$; space group = $P\bar{1}$; $a=7.5668(4)$, $b=9.6649(5)$, $c=16.0276(8)$ Å; $\alpha=84.406(2)$, $\beta=85.506(2)$, $\lambda=70.545(2)°$; $V=1098.63(10)$ Å^3; $Z=1$; $T=100(2)$ K; $\lambda=0.71073$ Å; $\rho_{calcd}=1.327$ g cm^{-3}; $\mu=1.243$ mm^{-1}; $R(F)=3.14\%$; $wR(F)=6.87\%$.

Complex ***6***: Formula = $C_{32}H_{56}N_4Br_4Cu_2$; $M_r=943.53$; space group = $P\bar{1}$; $a=7.4601(3)$, $b=10.0349(4)$, $c=14.1949(7)$ Å; $\alpha=100.620(2)$, $\beta=96.781(2)$, $\lambda=109.911(2)°$; $V=963.03(7)$ Å^3; $Z=1$; $T=100(2)$ K; $\lambda=0.71073$ Å; $\rho_{calcd}=1.627$ g cm^{-3}; $\mu=5.279$ mm^{-1}; $R(F)=2.33\%$; $wR(F)=5.12\%$.

Compression isotherms: The Π versus A isotherms were examined by using an automated KSF Minitrough at (22.8 ± 0.5) °C. Ultra-pure water with a resistivity of 17.5–18 MΩ cm^{-1} was obtained from a Barnstead NANOpure system and used in all experiments. Impurities present at the surface of the freshly poured aqueous subphase were removed by vacuum after compression of the barriers. Spreading solutions were prepared in spectroscopy-grade chloroform. A known quantity (typically 25 μL) of freshly prepared surfactant solution with a known concentration (1 mg mL^{-1}) was then spread on the clean aqueous subphase. The system was allowed to equilibrate for approximately 10 min before monolayer compression. The Π versus A isotherms were obtained at a compression rate of 10 mm min^{-1}. The Wilhelmy plate method (paper plates, 40 mm diameter) was used to measure the pressure.[54] At least three independent measurements were carried out per sample, with excellent reproducibility attained.

BAM studies: A KSV-Optrel BAM 300 equipped with a HeNe laser (10 mW, 632.8 nm) and a CCD detector was used for all micrographs. The compression rate was 10 mm min^{-1}, the field of view was 800 × 600 microns, and the lateral resolution was about 2–4 μm.

Electronic structure calculations: The B3LYP/6–311G(d) level of theory[55] was employed throughout to allow for the handling of negatively charged species. All calculations were done by using the Gaussian series of programs.[56] Geometries were fully minimized without symmetry constraints by using standard methods.[57] Located stationary points

were characterized by computing analytic vibrational frequencies. Reported energies include zero-point correction. Cartesian coordinates of all optimized structures are provided as supporting material.

Synthesis of the surfactants $L^{PyC_{18}}$, $L^{PyC_{16}}$, $L^{PyC_{14}}$, $L^{PyC_{10}}$: 2-Pyridinecarboxyaldehyde (1.07 g, 10 mmol) was treated with 1 equivalent of the appropriate alkylamine (1-octadecylamine, 1-hexadecylamine, 1-tetradecylamine, 1-decylamine) in methanol (50 mL). The resulting compounds were gently heated at reflux to give the equivalent imines, which were reduced in the presence of $NaBH_4$. The resulting compounds were obtained as off-white and waxy solids after being washed with CH_2Cl_2 and 5% $NaHCO_3$, then dried over Na_2SO_4 and recrystallized in acetone (yields = 78–84%). ^{1}H NMR (400 MHz, $CDCl_3$, 300 K): $\delta = 0.85$ ($1\times$t, 3×1H; CH_3), 1.20–1.50 (m, 32H, 28H, 24H, 16H, respectively; CH_2), 2.62 ($1\times$t, 2H; CH_2NH), 3.89 (s, 2×1H; Py–CH_2–NH), 7.14–7.61 (m, 3×1H; pyridine), 8.49 ppm (d, 1H; pyridine); IR (KBr): $\tilde{\nu} = 3306$ (s) (N–H_{amine}), 2920–2850 (C–H_{alkyl}), 1426–1484 cm^{-1} (s) (C=C_{Py}); ESIMS (MeOH): m/z: 361.3 [$L^{PyC_{18}}+H^+$]; 333.3 [$L^{PyC_{16}}+H^+$]; 305.3 [$L^{PyC_{14}}+H^+$]; 249.3 [$L^{PyC_{10}}+H^+$].

Synthesis of copper-containing surfactant complexes 1–3: Complexes **1–3** were all synthesized in a similar manner, in which the appropriate ligand (1.0 mmol) was treated with $CuCl_2{\cdot}2H_2O$ (0.183 g, 1 mmol; 1:1 ratio) in methanol (50 mL). The solution was kept under mild reflux, and gave a blue solution. Upon cooling, the complex was recrystallized from EtOH/$CHCl_3$ to give X-ray quality crystals that were used for structure determination.

*$[Cu^{II}Cl_2(L^{PyC_{18}})]$ (**1**)*: Yield 84%; m.p. 206–208°C; IR (KBr): $\tilde{\nu} = 2924$(s), 2849(s) (alkyl–CH–); 1380 (C=N_{Ar}, Ar = aromatic); 1606(s), 1573(m), 1468(s) (C=N_{Py}, C=C); ESIMS (MeOH): m/z (%): 458.2 (100) [Cu^{II}Cl-($L^{PyC_{18}}$)]$^+$; elemental analysis calcd (%) for $C_{24}H_{44}Cl_2CuN_2$: C 58.23, H 8.79, N 5.61; found: C 57.65, H 8.72, N 5.63.

*$[Cu^{II}Cl_2(L^{PyC_{16}})]$ (**2**)*: Yield 88%; m.p. 203–205°C; IR (KBr): $\tilde{\nu} = 2852$ (s), 2925 (s) (alkyl CH); 1610 (s), 1560 (m), 1472 (m) (C=N_{Py}, CH=CH); 1133 cm^{-1} (s) (R′–NH–R); ESIMS (MeOH): m/z (%): 430.2 (100) [Cu^{II}Cl($L^{PyC_{16}}$)]$^+$; elemental analysis calcd (%) for $C_{22}H_{40}Cl_2CuN_2$: C 56.58, H 8.63, N 6.00; found: C 56.48, H 8.35, N 5.82.

*$[Cu^{II}Cl_2(L^{PyC_{14}})]$ (**3**)*: Yield 78%; m.p. 204–205°C; IR (KBr): $\tilde{\nu} = 2854$ (s), 2925 (s) (alkyl CH); 1608 (s), 1564 (m), 1471 (m) (C=N_{Py}, CH=CH); 1130 cm^{-1} (s) (R′–NH–R); ESIMS (MeOH): m/z (%): 402.2 (100) [Cu^{II}Cl($L^{PyC_{14}}$)]$^+$; elemental analysis calcd (%) for $C_{20}H_{36}Cl_2CuN_2$: C 54.72, H 8.27, N 6.38; found: C 54.26, H 7.90, N 6.33.

Synthesis of copper-containing surfactant complexes 4–6: Complexes **4–6** were synthesized in a manner similar to that of **1–3**, except that $CuCl_2{\cdot}2H_2O$ was replaced by the salt $CuBr_2$ (1 mmol), and the resulting solution was green instead of blue. Upon recrystallization from *i*PrOH/$CHCl_3$, X-ray quality crystals of **6** were isolated.

*$[Cu^{II}Br_2(L^{PyC_{18}})]$ (**4**)*: Yield 87%; m.p. 172–174°C; IR (KBr): $\tilde{\nu} = 2850$ (s), 2920 (s) (alkyl CH); 1370 (C=N_{arom}); 1159 (s) (R′–NH–R); 1607 (s), 1573 (m), 1471 cm^{-1} (m) (C=N_{Py}, C=C); ESIMS (MeOH): m/z (%): 504.2 (100) [Cu^{II}Br($L^{PyC_{18}}$)]$^+$; elemental analysis calcd (%) for $C_{24}H_{44}Br_2CuN_2$: C 49.28, H 7.75, N 4.79; found: C 49.31, H 7.60, N 4.79.

*$[Cu^{II}Br_2(L^{PyC_{16}})]$ (**5**)*: Yield 83%; m.p. 170–172°C; IR (KBr): 2850 (s), 2922 (s) (alkyl CH_2); 1610 (s), 1569 (m), 1470 (m) (C=N_{Py}, C=C); 1150 cm^{-1} (s) (R′–NH–R); ESIMS (MeOH): m/z (%): 476.2 (100) [Cu^{II}Br($L^{PyC_{16}}$)]$^+$; elemental analysis calcd (%) for $C_{20}H_{36}Br_2CuN_2$: C 47.53, H 7.25, N 5.04; found: C 47.48, H 7.18, N 5.03.

*$[Cu^{II}Br_2(L^{PyC_{10}})]$ (**6**)*: Yield 76%; m.p. 142–143°C; IR (KBr): $\tilde{\nu} = 2834$ (s), 2931 (s) (alkyl CH); 1605 (s), 1568 (m), 1477 (m) (C=N_{Py}, CH=CH); 1127 cm^{-1} (s) (R′–NH–R); ESIMS (MeOH): m/z (%): 392.3 (100) [Cu^{II}Br($L^{PyC_{10}}$)]$^+$; elemental analysis calcd (%) for $C_{16}H_{28}Cl_2CuN_2$: C 40.73, H 5.98, N 5.94; found: C 41.02, H 5.80, N 4.56.

Acknowledgements

We gratefully acknowledge funding from the Nano@Wayne Initiative (Grant no. 11E420), the Donors of the ACS Petroleum Research Fund (Grant no. 42575-G3 for C.N.V.), and the National Science Foundation (Grant nos. 0718470 for C.N.V and 0553537 for S.R.P.R.). We also thank Prof. Bernhard Schlegel, WSU-Chemistry, for insightful discussions on the interpretation of the DFT calculations.

[1] a) R. A. Wassel, C. B. Gorman, *Angew. Chem.* **2004**, *116*, 5230; *Angew. Chem. Int. Ed.* **2004**, *43*, 5120; b) A. Dei, D. Gatteschi, C. Sangregorio, L. Sorace, *Acc. Chem. Res.* **2004**, *37*, 827; c) C. Joachim, J. K. Gimzewski, A. Aviram, *Nature* **2000**, *408*, 541.

[2] T. Govindaraju, P. J. Bertics, R. T. Raines, N. L. Abbott, *J. Am. Chem. Soc.* **2007**, *129*, 11223.

[3] D. R. Talham, *Chem. Rev.* **2004**, *104*, 5479.

[4] J. Park, A. N. Pasupathy, J. I. Goldsmith, C. Chang, Y. Yaish, J. R. Petta, M. Rinkoski, J. P. Sethna, H. D. Abruna, P. L. McEuen, D. C. Ralph, *Nature* **2002**, *417*, 722.

[5] a) J. Zhang, B. W.-K. Chu, N. Zhu, V. W.-W. Yam, *Organometallics* **2007**, *26*, 5423; b) V. W.-W. Yam, B. Li, Y. Yang, B. W.-K. Chu, K. M.-C. Wong, K.-K. Cheung, *Eur. J. Inorg. Chem.* **2003**, 4035; c) B. W.-K. Chu, V. W.-W. Yam, *Inorg. Chem.* **2001**, *40*, 3324.

[6] L. Boubekeur-Lecaque, B. J. Coe, K. Clays, S. Foerier, T. Verbiest, I. Asselberghs, *J. Am. Chem. Soc.* **2008**, *130*, 3286.

[7] K. Binnemans, Y. G. Galyametdinov, R. Van Deun, D. W. Bruce, S. R. Collinson, A. P. Polishchuk, I. Bikchantaev, W. Haase, A. V. Prosvirin, L. Tinchurina, I. Litvinov, A. Gubajdullin, A. Rakhmatullin, K. Uytterhoeven, L. Van Meervelt, *J. Am. Chem. Soc.* **2000**, *122*, 4335.

[8] J. B. Beck, S. J. Rowan, *J. Am. Chem. Soc.* **2003**, *125*, 13922.

[9] K. Binnemans, K. Lodewyckx, B. Donnio, D. Guillon, *Chem. Eur. J.* **2002**, *8*, 1101.

[10] a) P. C. Griffiths, I. A. Fallis, T. Chuenpratoom, R. Watanesk, *Adv. Colloid Interface Sci.* **2006**, *122*, 107; b) P. C. Griffiths, I. A. Fallis, D. J. Willock, A. Paul, C. L. Barrie, P. M. Griffiths, G. M. Williams, S. M. King, R. K. Heenan, R. Goergl, *Chem. Eur. J.* **2004**, *10*, 2022.

[11] I. Yildiz, J. Mukherjee, M. Tomasulo, F. M. Raymo, *Adv. Func. Mater.* **2007**, *17*, 814.

[12] a) J. W. Ciszek, Z. K. Keane, L. Cheng, M. P. Stewart, L. H. Yu, D. Natelson, J. M. Tour, *J. Am. Chem. Soc.* **2006**, *128*, 3179; b) J. M. Tour, *Acc. Chem. Res.* **2000**, *33*, 791.

[13] L. Kosbar, C. Srinivasan, A. Afzali, T. Graham, M. Copel, L. Krusin-Elbaum, *Langmuir* **2006**, *22*, 7631.

[14] For examples, see: a) M. C. Petty, *Langmuir–Blodgett Films: An Introduction*, Cambridge University Press, NY (USA), **1996**; b) R. H. Tredgold, *Order in Thin Organic Films*, Cambridge University Press, NY (USA), **1994**.

[15] X. Chen, S. Lenhert, M. Hirtz, N. Lu, H. Fuchs, L. Chi, *Acc. Chem. Res.* **2007**, *40*, 393.

[16] N. Nandi, D. Vollhardt, *Acc. Chem. Res.* **2007**, *40*, 351.

[17] A. Flores, P. Ize, S. Ramos, R. Castillo, *J. Chem. Phys.* **2003**, *119*, 5644.

[18] a) T. J. Joncheray, K. M. Denoncourt, C. Mathieu, M. A. R. Meier, U. S. Schubert, R. S. Duran, *Langmuir* **2006**, *22*, 9264; b) S. Peleshanko, J. Jeong, R. Gunawidjaja, V. V. Tsukruk, *Macromolecules* **2004**, *37*, 6511.

[19] I. Bury, B. Donnio, J.-L. Gallani, D. Guillon, *Langmuir* **2007**, *23*, 619.

[20] D. Hoenig, D. Moebius, *J. Phys. Chem.* **1991**, *95*, 4590.

[21] S. Hénon, J. Meunier, *Rev. Sci. Instrum.* **1991**, *62*, 936.

[22] C. M. Knobler, *Advances in Chemical Physics, Vol. 77*, (Eds.: I. Prigogine, S. A. Rice), Wiley, NY (USA), **1990**, p. 397.

[23] For examples, see: a) F. W. Vergeer, X. Chen, F. Lafolet, L. De Cola, H. Fuchs, L. Chi, *Adv. Funct. Mater.* **2006**, *16*, 625; b) P. Lehmann, C. Symietz, G. Brezesinski, H. Kra, D. G. Kurth, *Langmuir* **2005**, *21*, 5901; c) S. Di Bella, S. Sortino, S. Conoci, S. Petralia, S. Casilli, L. Valli, *Inorg. Chem.* **2004**, *43*, 5368; d) K. Wang, M.-A. Haga, M. D. Hossain, H. Shindo, K. Hasebe, H. Monjushiro, *Langmuir* **2002**, *18*, 3528.

[24] For earlier work on isolated and characterized metallosurfactants, see: D. A. Jaeger, M. F. Peacock, D. S. Bohle, *Langmuir* **2003**, *19*, 4859, and references [3] and [4] therein.
[25] R. Shakya, C. Imbert, H. P. Hratchian, M. Lanznaster, M. J. Heeg, B. R. McGarvey, M. Allard, H. B. Schlegel, C. N. Verani, *Dalton Trans.* **2006**, 2517.
[26] C. Imbert, H. P. Hratchian, M. Lanznaster, M. J. Heeg, L. M. Hryhorczuk, B. R. McGarvey, H. B. Schlegel, C. N. Verani, *Inorg. Chem.* **2005**, *44*, 7414.
[27] R. Shakya, S. S. Hindo, L. Wu, S. Ni, M. Allard, M. J. Heeg, S. R. P. da Rocha, G. T. Yee, H. P. Hratchian, C. N. Verani, *Chem. Eur. J.* **2007**, *13*, 9948.
[28] R. Shakya, S. S. Hindo, L. Wu, M. M. Allard, M. J. Heeg, H. P. Hratchian, B. R. McGarvey, S. R. P. da Rocha, C. N. Verani, *Inorg. Chem.* **2007**, *46*, 9808.
[29] S. S. Hindo, R. Shakya, N. S. Rannulu, M. M. Allard, M. J. Heeg, M. T. Rodgers, S. R. P. da Rocha, C. N. Verani, *Inorg. Chem.* **2008**, *47*, 3119.
[30] K. Nakamoto, *Infrared and Raman Spectra of Inorganic and Coordination Compounds*, 5th ed., Wiley, NY (USA), **1997**.
[31] M. Lanznaster, M. J. Heeg, G. T. Yee, B. R. McGarvey, C. N. Verani, *Inorg. Chem.* **2007**, *46*, 72.
[32] N. M. Villeneuve, R. R. Schroeder, L. A. Ochrymowycz, D. B. Rorabacher, *Inorg. Chem.* **1997**, *36*, 4475.
[33] R. Karmakar, C. R. Choudhury, D. L. Hughes, G. P. A. Yap, M. S. El Fallah, C. Desplanches, J.-P. Sutter, S. Mitra, *Inorg. Chim. Acta* **2006**, *359*, 1184.
[34] H. Nagao, N. Komeda, M. Mukaida, M. Suzuki, K. Tanaka, *Inorg. Chem.* **1996**, *35*, 6809.
[35] K. W. Pollak, J. W. Leon, J. M. J. Frechet, M. Maskus, H. D. Abruna, *Chem. Mater.* **1998**, *10*, 30.
[36] F. Barriere, W. E. Geiger, *J. Am. Chem. Soc.* **2006**, *128*, 3980.
[37] D. B. Rorabacher, *Chem. Rev.* **2004**, *104*, 651.
[38] M. Elleb, J. Meullemeestre, M. J. Schwing-Weill, F. Vierling, *Inorg. Chem.* **1980**, *19*, 2699.
[39] J. Foley, S. Tyagi, B. J. Hathaway, *J. Chem. Soc. Dalton Trans.* **1984**, 1.
[40] J. B. Peng, G. T. Barnes, I. R. Gentle, *Adv. Colloid Interface Sci.* **2001**, *91*, 163.
[41] S. Kraus, D. Mandler, *Langmuir* **2006**, *22*, 7462.
[42] A. Gericke, A. V. Michailov, H. Huehnerfuss, *Vib. Spectrosc.* **1993**, *4*, 335.
[43] J. Galvan-Miyoshi, S. Ramos, J. Ruiz-Garcia, R. Castillo, *J. Chem. Phys.* **2001**, *115*, 8178.
[44] A. Flores, E. Corvera-Poire, C. Garza, R. Castillo, *J. Phys. Chem. B* **2006**, *110*, 4824.
[45] G. Weidemann, D. Vollhardt, *Thin Solid Films* **1995**, *264*, 94.
[46] G. Gabrielli, G. Caminati, M. Puggelli, *Adv. Colloid Interface Sci.* **2000**, *87*, 75.
[47] U. Gehlert, D. Vollhardt, *Langmuir* **1997**, *13*, 277.
[48] A. Gopal, K. Y. C. Lee, *J. Phys. Chem. B* **2001**, *105*, 10348.
[49] T. Albright, J. K. Burdett, M.-H. Whangbo, *Orbital Interactions in Chemistry*, Wiley, NY (USA), **1985**.
[50] a) Reference [14a], p. 72; b) D. Möbius, *Ber. Bunsenges. Phys. Chem.* **1978**, *82*, 848.
[51] R. R. Gagne, C. A. Koval, G. C. Lisensky, *Inorg. Chem.* **1980**, *19*, 2854.
[52] *APEX II*, *SMART*, *SAINT*, and *SADABS*, Bruker AXS, Madison WI, USA, **2004**.
[53] G. Sheldrick, *Acta Cryst* **2008**, A64, 112.
[54] A. Gopal, V. A. Belyi, H. Diamant, T. A. Witten, K. Y. C. Lee, *Los Alamos Natl. Lab., Prepr. Arch., Condens. Matter* **2004**, arXiv:cond-mat/0409147.
[55] a) A. D. Becke, *Phys. Rev. A* **1988**, *38*, 3098; b) A. D. Becke, *J. Chem. Phys.* **1993**, *98*, 5648; c) T. Lee, W. T. Yang, R. G. Parr, *Phys. Rev.* **1988**, *B37*, 785; d) R. Ditchfield, W. R. Hehre, J. A. Pople, *J. Chem. Phys.* **1971**, *54*, 724; e) M. S. Gordon, *Chem. Phys. Lett.* **1980**, *76*, 163; f) P. C. Hariharan, J. A. Pople, *Theo. Chim. Acta.* **1973**, *28*, 213; g) P. C. Hariharan, J. A. Pople, *Mol. Phys.* **1974**, *27*, 209; h) W. R. Hehre, R. Ditchfield, J. A. Pople, *J. Chem. Phys.* **1972**, *56*, 225.
[56] Gaussian 03, Revision D.01, M. J. Frisch, G. W. Trucks, H. B. Schlegel, G. E. Scuseria, M. A. Robb, J. R. Cheeseman, J. A. Montgomery, Jr., T. Vreven, K. N. Kudin, J. C. Burant, J. M. Millam, S. S. Iyengar, J. Tomasi, V. Barone, B. Mennucci, M. Cossi, G. Scalmani, N. Rega, G. A. Petersson, H. Nakatsuji, M. Hada, M. Ehara, K. Toyota, R. Fukuda, J. Hasegawa, M. Ishida, T. Nakajima, Y. Honda, O. Kitao, H. Nakai, M. Klene, X. Li, J. E. Knox, H. P. Hratchian, J. B. Cross, V. Bakken, C. Adamo, J. Jaramillo, R. Gomperts, R. E. Stratmann, O. Yazyev, A. J. Austin, R. Cammi, C. Pomelli, J. W. Ochterski, P. Y. Ayala, K. Morokuma, G. A. Voth, P. Salvador, J. J. Dannenberg, V. G. Zakrzewski, S. Dapprich, A. D. Daniels, M. C. Strain, O. Farkas, D. K. Malick, A. D. Rabuck, K. Raghavachari, J. B. Foresman, J. V. Ortiz, Q. Cui, A. G. Baboul, S. Clifford, J. Cioslowski, B. B. Stefanov, G. Liu, A. Liashenko, P. Piskorz, I. Komaromi, R. L. Martin, D. J. Fox, T. Keith, M. A. Al-Laham, C. Y. Peng, A. Nanayakkara, M. Challacombe, P. M. W. Gill, B. Johnson, W. Chen, M. W. Wong, C. Gonzalez, J. A. Pople, Gaussian, Inc., Wallingford CT, **2004**.
[57] H. B. Schlegel, *J. Comput. Chem.* **1982**, *3*, 214.

Received: June 20, 2008
Published online: September 12, 2008

